Journal of
Materials Chemistry C

PAPER

View Article Online
View Journal | View Issue

Cite this: *J. Mater. Chem. C*, 2021, 9, 9907

A highly efficient purely organic room-temperature phosphorescence film based on a selenium-containing emitter for sensitive oxygen detection†

Shuai Wang,[ab] Haiyang Shu,[ab] Xianchao Han,[ab] Xiaofu Wu,[a] Hui Tong *[ab] and Lixiang Wang *[ab]

Received 20th May 2021,
Accepted 23rd June 2021

DOI: 10.1039/d1tc02324a

rsc.li/materials-c

Developing purely organic room-temperature phosphorescence (RTP) materials with high phosphorescence efficiency in film states is important for their applications but remains a great challenge. Herein, a donor–acceptor type RTP molecule (**SeX-CzPh**) with 9*H*-selenoxanthen-9-one and 9-phenyl-9*H*-carbazole as the acceptor and donor units, respectively, is designed and synthesized. **SeX-CzPh** shows a high phosphorescence quantum yield of 44.3% in a doped polystyrene film at room temperature, which is 4-fold higher than that of its analogue **TX-CzPh** with 9*H*-thioxanthene-9-one as the acceptor unit. The heavy selenium atom plays a key role in achieving high phosphorescence quantum yields, owing to the effective ISC process through strong spin–orbit coupling. Moreover, the **SeX-CzPh**-based oxygen film sensor exhibits a wide detection range (0–2.1 × 10^5 ppm), a high K_{SV} (1.27 × 10^{-4} ppm^{-1}) and a low detection limit (4.9 ppm). This work demonstrates that 9*H*-selenoxanthen-9-one is a promising building block for the rational design of highly efficient purely organic RTP materials.

Introduction

Room-temperature phosphorescence (RTP) materials have attracted great attention in recent years owing to their potential applications in sensing,[1,2] bioimaging,[3–5] anti-counterfeiting,[6–8] organic light-emitting diodes[9–11] and other optoelectronic devices.[12–15] Typically, highly efficient phosphorescence can be observed for inorganic or organometallic complexes due to the presence of Ir, Pt, Os and other heavy metals, which can promote spin–orbit coupling (SOC) and therefore intersystem crossing (ISC) between singlet and triplet states.[16,17] Unfortunately, the expensive and toxic heavy metals also severely limit their wide applications.[16–18] Recently, the development of purely organic, metal-free RTP molecules has been a hot topic of current interest because of their low toxicity and cost, versatile molecular design, facile functionalization, and good processability.[18,19] However, due to the spin-forbidden transition of triplet excitons, the long lifetime triplet excitons of purely organic molecules with weak SOC are prone to nonradiative deactivation *via* thermally vibrational and collisional processes or exposure to quenchers such as oxygen.[20,21] Therefore, most efficient RTP from purely organic molecules is only observed in their crystal or cocrystal states,[22–24] which may fix the molecular conformation through intermolecular interactions such as hydrogen bonding,[25] halogen bonding,[26,27] *etc.*, although the strict growth conditions and poor processability of organic crystals may restrict the development of RTP materials. In fact, the dispersion of light-emitting molecules in an amorphous polymer matrix is one of the most common methods for their real applications in optical device fabrication and processing; however, efficient RTP molecule-doped films are still rare, and in particular, most purely organic molecules with efficient RTP crystals are often poorly and even non-phosphorescent when dispersed in polymer films.[28] The enhancement of SOC to promote the ISC process is another way to improve the phosphorescence quantum yield (Φ_{Ph}) of metal-free RTP molecules. Halogen (Br, I), S and P atoms with external or internal heavy atom effects and organic moieties with lone-pair electrons, including aromatic aldehydes, ketones, sulfones, triazines, *etc.* and their combinations, have been widely used for the development of organic RTP molecules with good Φ_{Ph}.[29–31] Anyway, most of these efficient metal-free RTP molecules are still in crystal forms, which may limit their development and application.

Recently, selenium, a chalcogen atom with an atomic number (34) very close to that of the Br atom (35), has also been used to construct RTP molecules due to the heavy atom effect.[32–39]

---

[a] *State Key Laboratory of Polymer Physics and Chemistry, Changchun Institute of Applied Chemistry Chinese Academy of Sciences, Changchun, 130022, China. E-mail: chemtonghui@ciac.ac.cn, lixiang@ciac.ac.cn*

[b] *School of Applied Chemistry and Engineering, University of Science and Technology of China, Hefei, 230026, China*

† Electronic supplementary information (ESI) available. CCDC 2080394. For ESI and crystallographic data in CIF or other electronic format see DOI: 10.1039/d1tc02324a

For example, 10*H*-phenoselenazine (PSeZ)-based RTP molecules exhibit bright green phosphorescence (Φ_{Ph} up to 35%) when they are doped in a molecular n-type host, bis[2-(diphenylphosphino)-phenyl]ether oxide (DPEPO).[37] Interestingly, donor–acceptor (D–A) type molecules with the PSeZ donor unit can display both thermally activated delayed fluorescence (TADF) and phosphorescence due to different conformers. Red phosphorescence emission is also observed for a perselenated benzene with a Φ_{Ph} of 21% in the solid state. A carbazolyl derivative containing a selenophene unit shows orange-red phosphorescence (Φ_{Ph} = 7.0%) in the crystal state.[38] In all these cases, the presence of Se can strengthen SOC and ISC for phosphorescence due to the heavy atom effect. Particularly, the embedded Se in the core structures of RTP molecules is believed to be more helpful for SOC enhancement than a simple substituent such as Br. Thus, the combination of the aromatic ketone and the nonmetallic Se atom into a conjugated core structure is envisioned to construct highly efficient RTP molecules.

In this contribution, we report a D–A type RTP molecule (**SeX-CzPh**) with 9*H*-selenoxanthen-9-one (SeX) and 9-phenyl-9*H*-carbazole as the acceptor and donor units, respectively (Scheme 1). The presence of both the heavy Se atom and the ketone group with lone-pair electrons in the SeX ring may facilitate the ISC process through strong SOC to result in efficient phosphorescence. At the same time, the formation of a moderately twisted D–A structure can reduce the spatial overlap between the highest occupied molecular orbital (HOMO) and the lowest unoccupied molecular orbital (LUMO) and obtain a small energy gap (ΔE_{ST}) between the S_1 and T_1 excited states. Compared to **TX-CzPh** with 9*H*-thioxanthene-9-one as the acceptor unit, **SeX-CzPh** exhibits a much higher RTP quantum yield in a doped polystyrene (PS) film. Both experimental and theoretical investigations reveal that the high-efficiency RTP of the **SeX-CzPh** doped film is mainly ascribed to the higher RTP radiative rate and ISC rate. The **SeX-CzPh** doped film has also been used as a film-sensor for detection of oxygen, which exhibits a highly sensitive and reversible oxygen sensing performance.

Results and discussion

The synthesis routes for **SeX-CzPh** are shown in Scheme 1.[28,40] First, the reaction of 3-bromobenzoic acid with diphenyl diselenide was catalyzed by a ruthenium(II) catalyst, followed by treatment with trifluoromethanesulfonic acid to give **SeX–Br**. **SeX-CzPh** was obtained by the palladium-catalyzed Suzuki coupling between **SeX–Br** and (9-phenyl-9*H*-carbazol-3-yl)boronic acid in a yield of 61%. 2-(9-phenyl-9*H*-carbazol-3-yl)-9*H*-thioxanthene-9-one (**TX-CzPh**) was also prepared by a similar method (Scheme 1). The structures of both compounds were proved by the combination of ^{1}H and ^{13}C NMR spectroscopy and mass spectrometry (Fig. S1–S3, ESI†).

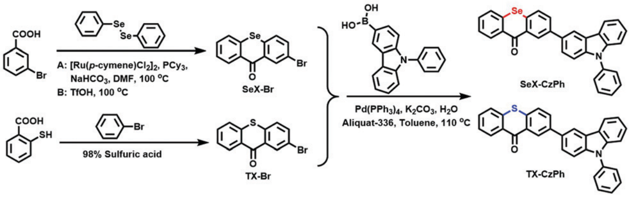

Scheme 1 Synthetic routes for **SeX-CzPh** and **TX-CzPh**.

The photophysical properties of **SeX-CzPh** and **TX-CzPh** were investigated (Fig. 1 and Table 1). In toluene solution, both **SeX-CzPh** and **TX-CzPh** show similar absorption spectra with strong absorption peaks at 308 nm and weak absorption bands around 400 nm (Fig. S4a and S5a, ESI†). Although no clear luminescence can be observed for their solutions, the **SeX-CzPh** (1 wt%) doped polystyrene (PS) film exhibits bright green emission with an emission peak at 500 nm and a shoulder peak at 453 nm in a vacuum at room temperature (Fig. 1a). When the film was exposed to air, the PL intensity significantly decreased (Fig. 1b). The air-sensitive PL emission of the **SeX-CzPh** doped film suggests that triplet excitons may be involved in the luminescence process, and oxygen may act as aquencher of triplet excitons. At a low temperature of 77 K, the delayed emission spectrum with a delay time of 1 ms of the **SeX-CzPh** doped film retains the emission peak at 500 nm, while that at 453 nm disappears completely, suggesting that the emission peaks at 500 nm and 453 nm could be ascribed to the phosphorescence and fluorescence emissions, respectively (Fig. 1c). Time-resolved photoluminescence experiments further reveal that the different lifetimes in the long-wavelength and short-wavelength regions at room temperature are 1.62 ms (500 nm) and 1.08 ns (453 nm), respectively (Fig. 1d). Moreover, the lifetime in milliseconds is temperature-dependent and decreases with the increasing temperature (Fig. S4b, ESI†). These results indicate that the **SeX-CzPh** doped film has a dual-emissive

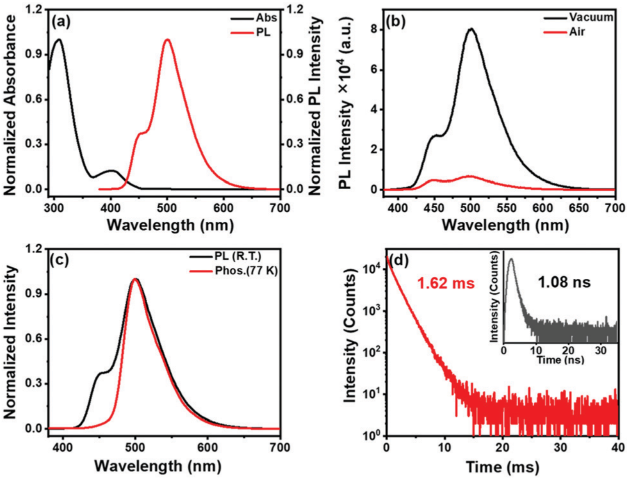

Fig. 1 (a) UV-vis spectrum (black) in air and steady-state PL spectrum (red) of the **SeX-CzPh** doped film in vacuum at room temperature; (b) steady-state PL spectra of the **SeX-CzPh** doped film in vacuum (black) and in air (red) at room temperature; (c) steady-state PL spectrum (black) at room temperature and delayed spectrum (red) at 77 K (delay time: 1 ms) of the **SeX-CzPh** doped film; (d) time-resolved PL decay spectra measured at 500 nm and 453 nm (inset) of the **SeX-CzPh** doped film at room temperature.

Table 1 Summary of the photophysical properties of **SeX-CzPh** and **TX-CzPh**

Compound	λ_{PL} [nm]	Φ_{PL} [%]	Φ_{FL} [%]	Φ_{Ph} [%]	τ_{FL} [ns]	τ_{Ph} [ms]	k_r^F [$\times 10^7$ s^{-1}]	k_{ISC} [$\times 10^8$ s^{-1}]	k_r^P [$\times 10^2$ s^{-1}]	$k_{nr}^P + k_q$ [$\times 10^2$ s^{-1}]
SeX-CzPh	453, 500	48.1	3.8	44.3	1.08	1.62	3.5	8.9	2.8	3.3
TX-CzPh	441, 487	21.9	11.8	10.1	1.35	10.38	8.7	6.5	0.1	0.9

property of strong RTP and weak fluorescence. On the other hand, the **TX-CzPh** doped film emits blue light, and exhibits a dominant peak at 441 nm with a lifetime of 1.35 ns and a shoulder peak at 487 nm with a lifetime of 10.38 ms, corresponding to the fluorescence and phosphorescence emissions, respectively (Fig. S5c and d, ESI†). It is noted that the **SeX-CzPh** doped film has a high photoluminescence quantum yield (Φ_{PL}) of 48.1%, which is two times higher than that of the **TX-CzPh** doped film (21.9%). Particularly, the phosphorescence quantum yield (Φ_{Ph}) of the **SeX-CzPh** doped film is up to 44.3%, which is four times higher than that of the **TX-CzPh** doped film (Φ_{Ph} = 10.1%), indicating that the introduction of the selenium atom enhances the RTP emission dramatically. To the best of the authors' knowledge, the Φ_{Ph} of 44.3% is not only the highest value for selenium-containing RTP materials, but also among the best results for purely organic RTP-doped films (Table S1, ESI†).[37,41–46]

To better understand the exciton dynamic process, the radiative rate constants of fluorescence (k_r^F) and phosphorescence (k_r^P), the intersystem crossing rate constant (k_{ISC}), and the sum of the nonradiative constant of phosphorescence (k_{nr}^P) and the quenching rate of T_1 (k_q) of the **SeX-CzPh** and **TX-CzPh** doped films were calculated according to eqn (S1)–(S8) (ESI†). As shown in Table 1, when the sulfur atom is replaced by the selenium atom, k_{ISC} is increased 1.5-fold, and k_r^P is increased by two orders of magnitude. The larger k_{ISC} and k_r^P allow for more efficient phosphorescence radiation and ISC process, leading to a higher Φ_{Ph} for the **SeX-CzPh** doped film.

The photophysical properties of the **SeX-CzPh** crystal powder were also investigated. Relative to the doped film, the crystal powder of **SeX-CzPh** shows red-shifted emission peaks at 483 nm and 543 nm, respectively, and thus emits yellow light at room temperature. At 77 K, the delayed emission spectrum with a delay time of 0.5 ms of the **SeX-CzPh** crystal powder retains the emission peak at 543 nm, while that at 483 nm disappears completely (Fig. 2a). The lifetime of the **SeX-CzPh** crystal powder also shortens to 0.79 ns and 15.74 μs, respectively (Fig. 2b and Fig. S6, ESI†). The temperature-dependent lifetime of the long-wavelength emission also decreases with the increasing temperature, confirming that the **SeX-CzPh** crystal powder shows RTP emission at 543 nm and fluorescence emission at 483 nm (Fig. 2b). Unlike the common organic RTP molecules in which crystallization enhances phosphorescence emission, the Φ_{Ph} of the **SeX-CzPh** crystal powder is only 2.9%, which is one-fifteenth of that of the doped film (44.3%). To reveal the essence of low-efficiency RTP in the **SeX-CzPh** crystal powder, the k_{ISC}, k_r^P and $k_{nr}^P + k_q$ of the **SeX-CzPh** crystal powder were also calculated (Fig. 3d and Table S2, ESI†). Although k_r^P and k_{ISC} of the **SeX-CzPh** crystal powder are nearly 7-fold and 1.4-fold higher than those of the **SeX-CzPh** doped film, respectively, the $k_{nr}^P + k_q$ is 200-fold higher than that of the doped film. As a result, **SeX–CzxPh** in the crystal powder state has a dramatically increased non-radiative loss of triplet excitons, leading to the reduced Φ_{Ph}.

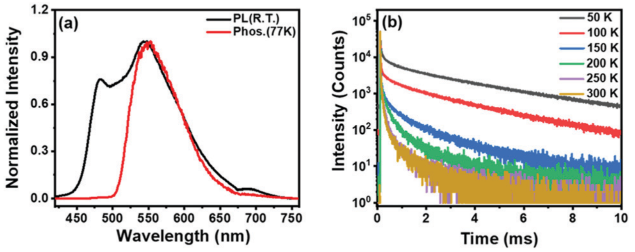

Fig. 2 (a) Steady-state PL spectrum (black) at room temperature and delayed PL spectrum (red) at 77 K (delay time: 1 ms) of the **SeX-CzPh** crystal powder; (b) temperature-dependent time-resolved PL decay spectra of the **SeX-CzPh** crystal powder at 543 nm.

To gain deep insights into the solid-state luminescence behavior, a single crystal of **SeX-CzPh** was cultivated by a solvent diffusion method at room temperature using toluene as a good solvent and ether as a poor solvent (Fig. 3 and Table S5, ESI†).

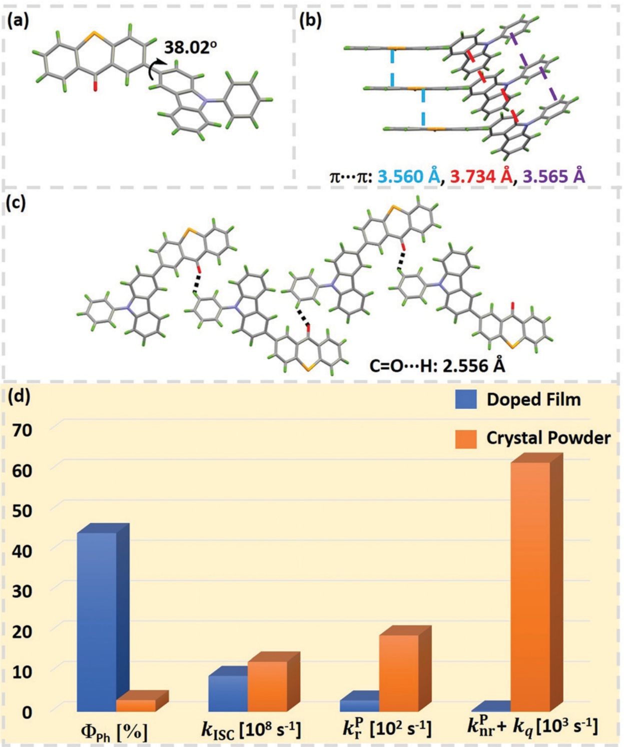

Fig. 3 (a) Molecular structure, (b) intermolecular π–π stacking and (c) intermolecular hydrogen bond interaction in the **SeX-CzPh** single crystal; (d) the comparison of photophysical constants between the doped film and the crystal powder of **SeX-CzPh**.

The **SeX-CzPh** monomer exhibits a twisted structure between the SeX acceptor plane and the carbazole donor plane with a twist angle of 38.02°. Such a moderately twisted D–A configuration reduces the spatial overlap between the HOMO and LUMO and facilitates a small energy gap (ΔE_{ST}) between the S_1 and T_1 excited states, which can promote the ISC process. In the **SeX-CzPh** crystal, C–H···O═C hydrogen bonds are formed between the carbonyl groups and the phenyl groups in adjacent molecules and the hydrogen bond interaction distance is 2.556 Å (Fig. 3c). The rigid and planar conjugated fragments, including SeX, carbazole and benzene, induced compact π–π stacking with the interaction distances of 3.560 Å, 3.734 Å and 3.565 Å (Fig. 3b), respectively. Multiple and strong π–π interactions may intensify emission quenching, and thus reduce the Φ_{PL} of the **SeX-CzPh** crystal powder.

In order to clarify the role of the heavy selenium atom, the frontier orbital distribution, the excited state energy and the SOC constants were calculated. Both **SeX-CzPh** and **TX-CzPh** have similar geometric configurations with torsion angles of 36.80° and 36.10° between SeX or TX and the carbazole moiety, respectively (Fig. S10, ESI†). The LUMOs of **SeX-CzPh** and **TX-CzPh** are completely located on the SeX and TX fragments, while the HOMOs are mainly distributed on the carbazole fragments and extended to the SeX and TX parts, indicating that the HOMO and LUMO are partially separated and facilitate a small energy gap to promote the ISC process (Fig. S10, ESI†). According to TD-DFT calculations, the two emitters exhibited similar distribution patterns of excited states with five triplet states (T) below their singlet states (S_1). The energy gap between S_1 and T_1 for **SeX-CzPh** is ΔE_{ST} = 0.69 eV and **TX-CzPh** is ΔE_{ST} = 0.67 eV. Compared with **TX-CzPh**, **SeX-CzPh** has slightly lower S_1 and T_1 energy levels (Fig. 4 and Tables S6, S8, ESI†), which is consistent with the red-shifted emission of **SeX-CzPh**. Although **SeX-CzPh** and **TX-CzPh** have similar geometric configurations, electronic configurations and excited state energies and energy gap between S_1 and T_1, their SOC constants are remarkably different (Fig. 4 and Tables S7, S9, ESI†). According to the El-Sayed rule, when the electronic configuration of the S_1 state is $^1(n, \pi^*)$ and the electronic configuration of the T_1 state is $^3(\pi, \pi^*)$, or when that of the S_1 state is $^1(\pi, \pi^*)$ and that of the T_1 state is $^3(n, \pi^*)$, the ISC process will be effective. In the **SeX-CzPh** and **TX-CzPh** monomers, the ISC process is from $^1(n, \pi^*)$ to $^3(\pi, \pi^*)$, which means that both **SeX-CzPh** and **TX-CzPh** can realize ISC and radiate phosphorescence effectively (Fig. S11, ESI†).

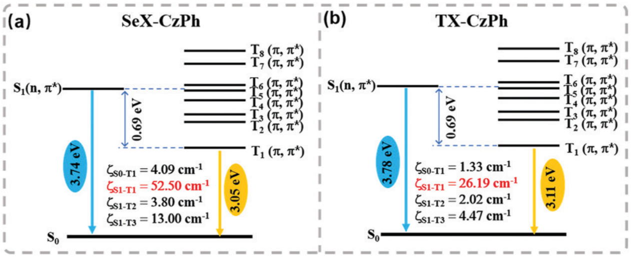

Fig. 4 The comparison of calculated SOC and energy level diagram of (a) **SeX-CzPh** and (b) **TX-CzPh**.

For the ISC process of S_1–T_n, the maximum SOC constant of **SeX-CzPh** is 52.50 cm^{-1} (from S_1 to T_1), which is two times higher than that of **TX-CzPh** (S_1–T_1: 26.19 cm^{-1}). The much larger S_1–T_1 SOC constant of **SeX-CzPh** ensures a more efficient ISC process from S_1 to T_1, and thus higher triplet exciton yield. For the phosphorescence radiation process of S_0–T_1, the SOC constant of **SeX-CzPh** is 4.09 cm^{-1}, three times higher than that of **TX-CzPh** (1.33 cm^{-1}), which accelerates the radiative transition process from T_1 to S_0. The larger SOC constants of the **SeX-CzPh** monomer indicate that the replacement of the sulfur atom with the selenium atom makes the ISC and phosphorescence radiation processes more effective, which is also consistent with the higher k_r^p and RTP quantum yield of the **SeX-CzPh** doped film.

Since oxygen can quench the triplet excitons of phosphorescent emitters through energy transfer, RTP materials are usually used for the detection of oxygen. Considering the oxygen-sensitive RTP emission of **SeX-CzPh** and **TX-CzPh**, optical film sensors for oxygen were made by doping **SeX-CzPh** and **TX-CzPh** into PS. As shown in Fig. 5 and Table S4 (ESI†), the emission intensity of both the **SeX-CzPh** and **TX-CzPh** doped films gradually decreases with the increasing oxygen content. When the oxygen fraction reaches 2.1 × 10^5 ppm (21%), the emission of the **SeX-CzPh** film at 500 nm is quenched 27.6-fold (Fig. 5a), while that of the **TX-CzPh** film is only quenched 5.3-fold (Fig. 5b), indicating the higher quenching efficiency of the **SeX-CzPh** film. The **SeX-CzPh** film showed a wide linear response range of oxygen concentrations from 0 to 2.1 × 10^5 ppm. According to the Stern–Volmer relation: $I_0/I - 1 = K_{SV}\,[O_2]$, the plot could be linearly fitted (R^2 = 0.99687), and the Stern–Volmer constant (K_{SV}) is calculated to be 1.27 × 10^{-4} ppm^{-1} (Fig. 5c). The limit of detection (LOD) of **SeX-CzPh** is 4.9 ppm. On the other hand, the **TX-CzPh** film has a narrower linear region (0 to 4.0 × 10^4 ppm) with a slightly lower K_{SV} of 1.08 × 10^{-4} ppm^{-1} and

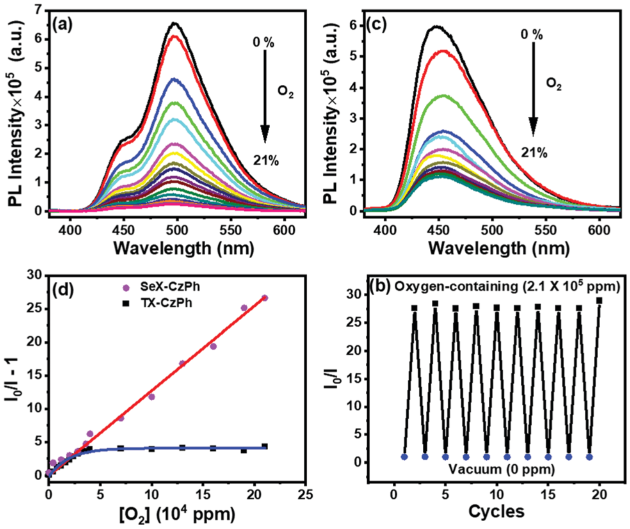

Fig. 5 (a) PL spectra of the **SeX-CzPh** doped film at different concentrations of oxygen; (b) PL spectra of the **TX-CzPh** doped film at different concentrations of oxygen; (c) Stern–Volmer quenching plots for **SeX-CzPh** and **TX-CzPh** by oxygen; (d) reversible oxygen response of the **SeX-CzPh** doped film.

a higher LOD of 10.7 ppm. These results demonstrate that the introduction of the selenium atom is favorable for enhancing the sensing performance. Compared with the oxygen sensors based on phosphorescent materials reported previously, the **SeX-CzPh** film displays a more comprehensive performance with a wide linear response range and high sensitivity simultaneously, which is more conducive to the application of oxygen sensing (Table S4, ESI†).[47–52] Besides, to evaluate the reversible sensing ability of **SeX-CzPh** for oxygen, the phosphorescence intensity at 500 nm of the **SeX-CzPh** doped film was monitored when alternately placing the doped film into a vacuum environment and an environment containing oxygen ($[O_2]$ = 21%). The emission of the **SeX-CzPh** doped film quenched by oxygen can be fully restored and the process could be repeated at least ten times (Fig. 5d).

Conclusion

In conclusion, a D–A type RTP molecule, **SeX-CzPh,** consisting of the 9*H*-selenoxanthen-9-one (SeX) acceptor unit and the 9-phenyl-9*H*-carbazole donor unit was synthesized. The **SeX-CzPh** doped film shows bright fluorescence–phosphorescence dual emission with a high Φ_{PL} of 48.1% at room temperature. In particular, compared with its analogue, **TX-CzPh,** with the 2-(9-phenyl-9*H*-carbazol-3-yl)-9*H*-thioxanthene-9-one acceptor, its RTP quantum yield of 44.3% is four times higher than that of the **TX-CzPh** doped film (10.1%), which is not only the highest value for selenium-containing purely organic RTP materials, but also among the best results for purely organic RTP-doped films. The high RTP quantum yield of the **SeX-CzPh** doped film could be ascribed to the introduction of the heavy selenium atom, which promotes the ISC and phosphorescence radiation processes. The **SeX-CzPh** doped film exhibits a highly sensitive and reversible oxygen sensing performance with a wider detection range (0–2.1×10^5 ppm), a higher K_{SV} (1.27×10^{-4} ppm^{-1}) and a lower detection limit (4.9 ppm), which are superior to those of the **TX-CzPh** doped film. These results demonstrate that 9*H*-selenoxanthen-9-one is a promising building block for the rational designof RTP materials with high phosphorescence efficiency in film states, and holds great potential for sensing applications.

Experimental

Measurements and characterization

The ^{1}H-NMR and ^{13}C-NMR spectra were recorded using a 500 MHz Bruker Avance NMR spectrometer with tetramethylsilane (TMS) as an internal standard. The MALDI-TOF mass spectra were recorded using an AXIMA CFR MS apparatus (COMPACT). The UV-Vis absorption spectra were recorded using a PerkinElmer Lambda 35 UV-Vis spectrometer. The photoluminescence (PL) measurements were conducted using a FluoroMax-4 spectrophotometer equipped with a 150 W xenon lamp as the excitation source. The fluorescence and phosphorescence lifetimes were measured with an Edinburgh fluorescence spectrometer (FLSP-980). The quantum yields were measured using an integrating sphere (Hamamatsu Photonics C9920-2). The preparation process of the **SeX-CzPh** (1 wt%) doped film is as follows: **SeX-CzPh**/PS (weight ratio = 1/99) was dissolved in toluene solution (1 mg mL^{-1} in total) and stirred for 30 min at room temperature in a glovebox. Then, the mixed solution was spin-coated onto quartz substrates at 1000 rpm for 3 min to obtain the doped film. The **TX-CzPh** (1 wt%) doped film was also prepared in the same way. The single-crystal X-ray diffraction experiments were carried out using a Bruker Smart APEX diffractometer with a CCD detector, graphite monochromator, and Mo Kα radiation (λ = 0.71073 Å) at 301 K. The intensity data were recorded with the ω scan mode. The Lorentz polarization factors were determined for the intensity data and the absorption corrections were performed using the SADABS program. The crystal structure was determined by using the SHELXTL program and refined by using the full matrix least squares method. All the non-hydrogen atoms were assigned with anisotropic displacement parameters, whereas the hydrogen atoms were placed at the calculated positions theoretically and included in the final cycles of refinement in a riding model along with the attached carbons.

Materials

All the chemicals and reagents were used as received from commercial sources without further purification. Solvents for chemical synthesis were purified according to standard procedures.

Synthesis of 2-bromo-9*H*-selenoxanthen-9-one (SeX–Br)

3-Bromobenzoic acid (1 g, 4.97 mmol), 1,2-diphenyldiselane (3.12 g, 9.94 mmol), [Ru(*p*-cymene)$Cl_2]_2$ (130 mg, 0.20 mmol), PCy_3 (112 mg, 0.4 mmol), and $NaHCO_3$ (420 mg, 4.97 mmol) were dissolved in dry DMF (40 mL) under air, and the resulting mixture was heated at 100 °C for 48 h. The colour changes from orange to deep-red and then becomes black. Acetic acid was added to adjust the solution to acidity, and then diluted with water. The mixture was extracted with ethyl acetate, and then washed with saturated brine. After the organic layer was dried over anhydrous $NaSO_4$, the solvent was removed under vacuum. The residue was purified by silica gel column chromatography (hexane : ethyl acetate : acetic acid = 90 : 10 : 1) to get the crude product, which was further treated with triflic acid at 100 °C for 5 h. After cooling to room temperature, the reaction was quenched with water, and then extracted with dichloromethane (DCM). The organic layer was dried over anhydrous Na_2SO_4 and concentrated under reduced pressure. The resulting residue was purified by silica gel column chromatography (hexane : dichloromethane = 4 : 1) to provide a yellow solid (1.02 g, 61%). ^{1}H NMR (500 MHz, $CDCl_3$) δ (ppm): 8.78 (d, J = 1.8 Hz, 1H), 8.65 (dd, J = 6.5 Hz, J = 1.1 Hz, 1H), 7.67–7.62 (m, 2H), 7.57 (td, J = 6.1 Hz, J = 1.2 Hz, 1H), 7.53 (d, J = 6.7 Hz, 1H), 7.51–7.47 (m, 1H). MALDI-TOF MS (*m*/*z*): 338.1 [M$^+$].

Synthesis of 2-bromo-9*H*-thioxanthen-9-one (TX-Br)

α-Mercaptobenzoic acid (5.4 g, 0.035 mol) was added portion-wise to a mixture of concentrated sulfuric acid (50 mL, 98%) and excess bromobenzene (7.3 mL, 0.07 mol). The resulting suspension was stirred at room temperature for 24 hours, and then permitted to stand for an additional 1 hour at 100 °C. The colour rapidly changes from yellow to deep-red. The mixture was cooled and poured slowly over ice, filtered, and washed with water. After being extracted with chloroform, the combined organic layer was dried over anhydrous Na_2SO_4. After the removal of solvent, the crude product was further purified by column chromatography on silica gel (dichloromethane : petroleum ether = 1 : 5) as the eluent. The product was isolated as a yellow solid (6.51 g, 64%). ^{1}H NMR (500 MHz, $CDCl_3$) δ (ppm): 8.75 (d, J = 2.2 Hz, 1H), 8.62 (dd, J = 8.1 Hz, J = 1.2 Hz, 1H), 7.72 (dd, J = 8.6 Hz, J = 2.2 Hz, 1H), 7.68–7.62 (m, 1H), 7.61–7.57 (m, 1H), 7.54–7.46 (m, 2H). MALDI-TOF MS (*m*/*z*): 291.2 [M^+].

Synthesis of 2-(9-phenyl-9*H*-carbazol-3-yl)-9*H*-selenoxanthen-9-one (SeX-CzPh)

2-Bromo-9*H*-selenoxanthen-9-one (500 mg, 1.48 mmol), (9-phenyl-9*H*-carbazol-3-yl)boronic acid (637 mg, 2.22 mmol), $Pd(PPh_3)_4$ (85.47 mg, 0.074 mmol), 2 M K_2CO_3 (5 mL), and Aliquant-336 (two drops) were dissolved in dry toluene (25 mL) under argon. The resulting mixture was heated at 110 °C for 12 h. After cooling to room temperature, dichloromethane was added and the mixture was washed with water. The organic layer was dried over anhydrous Na_2SO_4, and then the solvent was removed under vacuum. The resulting residue was purified by silica gel column chromatography (hexane : dichloromethane = 6 : 1) to provide a pure yellow solid (460 mg, 62%). ^{1}H NMR (500 MHz, $CDCl_3$,) δ (ppm): 9.04 (d, J = 1.7 Hz, 1H), 8.71 (dd, J = 6.4 Hz, J = 1.3 Hz, 1H), 8.48 (d, J = 1.4 Hz, 1H), 8.23 (d, J = 6.2 Hz, 1H), 7.95 (dd, J = 6.6 Hz, J = 1.8 Hz, 1H), 7.78–7.73 (m, 2H), 7.68 (dd, J = 6.3 Hz, J = 1.0 Hz, 1H), 7.66–7.62 (m, 2H), 7.62–7.59 (m, 2H), 7.57 (td, J = 6.0 Hz, J = 1.3 Hz, 1H), 7.53–7.48 (m, 3H), 7.47–7.42 (m, 2H), 7.34 (m, 1H). ^{13}C NMR (126 MHz, $CDCl_3$) δ (ppm): 182.22, 141.42, 140.65, 140.64, 137.53, 135.10, 132.98, 132.19, 131.67, 131.53, 131.17, 131.15, 130.99, 129.97, 129.35, 128.82, 128.40, 127.63, 127.09, 126.80, 126.29, 125.24, 124.06, 123.37, 120.50, 120.25, 118.86, 110.25, 109.98. MALDI-TOF MS (*m*/*z*): 501.1 [M^+].

Synthesis of 2-(9-phenyl-9*H*-carbazol-3-yl)-9*H*-thioxanthen-9-one (TX-CzPh)

2-Bromo-9*H*-thioxanthen-9-one (500 mg, 1.71 mmol), (9-phenyl-9*H*-carbazol-3-yl) boronic acid (500 mg, 1.74 mmol), $Pd(PPh_3)_4$ (99 mg, 0.086 mmol), 2 M K_2CO_3 (5 mL), and Aliquant-336 (two drops) were dissolved in dry toluene (25 mL) under argon. The resulting mixture was heated at 110 °C for 12 h. After cooling to room temperature, dichloromethane was added and the mixture was washed with water. The organic layer was dried over anhydrous Na_2SO_4, and the solvent was removed under vacuum. The resulting residue was purified by silica gel column chromatography (hexane : dichloromethane = 6 : 1) to provide a pure yellow solid (475 mg, 61%). ^{1}H NMR (500 MHz, $CDCl_3$) δ (ppm): 9.00 (d, J = 1.7 Hz, 1H), 8.68 (dd, J = 6.4 Hz, J = 1.1 Hz, 1H), 8.49 (d, J = 1.4 Hz, 1H), 8.23 (d, J = 6.1 Hz, 1H), 8.03 (dd, J = 6.7 Hz, J = 1.7 Hz, 1H), 7.77 (dd, J = 6.8 Hz, J = 1.5 Hz, 1H), 7.70 (d, J = 6.7 Hz, 1H), 7.67–7.58 (m, 6H), 7.54–7.48 (m, 3H), 7.47–7.42 (m, 2H), 7.34 (m, 1H). ^{13}C NMR (126 MHz, $CDCl_3$) δ (ppm): 141.42, 140.67, 140.16, 137.52, 137.32, 135.24, 132.25, 131.58, 131.33, 129.99, 129.97, 129.54, 129.25, 127.67, 127.63, 127.09, 126.56, 126.30, 126.09, 125.26, 124.07, 123.38, 120.50, 120.26, 118.90, 110.26, 109.99. MALDI-TOF MS (*m*/*z*): 453.1 [M^+].

Theoretical calculations

The density functional theory (DFT) and time-dependent density functional theory (TD-DFT) calculations were carried out at the M062X/def2SV level using the Gaussian 09 package. **SeX-CzPh** and **TX-CzPh** were directly optimized to obtain the S_0 geometry using a solvent model. The TD-DFT calculations for all molecules were performed using the optimized S_0 geometry. The orbital coupling constant (SOC) was determined at the M062X/def2SV level using on ORCA 4.2.1. The SOC was calculated using the optimized S_0 geometry. The hole–electron analysis of **SeX-CzPh** and **TX-CzPh** was carried out using Multiwfn 3.7.

Oxygen sensing

The steady-state spectra and PL intensity were recorded using a FluoroMax-4 spectrophotometer equipped with a 150 W xenon lamp as the excitation source. A series of different oxygen fractions were prepared by controlling the flow rate of high-purity oxygen and high-purity nitrogen using a flow control valve. The PL quenching experiment of the **SeX-CzPh** and **TX-CzPh** doped films was carried out by sequentially introducing different ratios of oxygen/argon mixed gas into the closed system. The oxygen concentrations were analyzed quantitatively according to the Stern–Volmer eqn (1):

$$I_0/I - 1 = K_{SV}[O_2] \tag{1}$$

here I_0 denotes the initial emission intensity of the film in a fully deoxygenated state, and I denotes the emission intensity of the film changed with different fractions of oxygen; K_{SV} is the Stern–Volmer constant; $[O_2]$ is the oxygen fraction. The LOD is defined as the concentration at which $I_0 - I$ is equal to 3-fold S/N (signal-to-noise ratio). 1 ppm O_2 corresponds to 0.0001% O_2 (ratio by volume).

Conflicts of interest

There are no conflicts to declare.

Acknowledgements

This work was financially supported by the National Natural Science Foundation of China (Grant No. 22075272, 51833009, 91833306, 51973211 and 21674111).

Notes and references

1 Y. Han, Y. You, Y.-M. Lee and W. Nam, *Adv. Mater.*, 2012, **24**, 2748–2754.

2 D. Lee, O. Bolton, B. C. Kim, J. H. Youk, S. Takayama and J. Kim, *J. Am. Chem. Soc.*, 2013, **135**, 6325–6329.

3 Z. He, H. Gao, S. Zhang, S. Zheng, Y. Wang, Z. Zhao, D. Ding, B. Yang, Y. Zhang and W. Z. Yuan, *Adv. Mater.*, 2019, **31**, 1807222.

4 X. Zhen, Y. Tao, Z. An, P. Chen, C. Xu, R. Chen, W. Huang and K. Pu, *Adv. Mater.*, 2017, **29**, 1606665.

5 Y. Mu, Z. Yang, J. Chen, Z. Yang, W. Li, X. Tan, Z. Mao, T. Yu, J. Zhao, S. Zheng, S. Liu, Y. Zhang, Z. Chi, J. Xu and M. P. Aldred, *Chem. Sci.*, 2018, **9**, 3782–3787.

6 X. Wang, H. Ma, M. Gu, C. Lin, N. Gan, Z. Xie, H. Wang, L. Bian, L. Fu, S. Cai, Z. Chi, W. Yao, Z. An, H. Shi and W. Huang, *Chem. Mater.*, 2019, **31**, 5584–5591.

7 S. Cai, H. Shi, J. Li, L. Gu, Y. Ni, Z. Cheng, S. Wang, W.-W. Xiong, L. Li, Z. An and W. Huang, *Adv. Mater.*, 2017, **29**, 1701244.

8 Z. An, C. Zheng, Y. Tao, R. Chen, H. Shi, T. Chen, Z. Wang, H. Li, R. Deng, X. Liu and W. Huang, *Nat. Mater.*, 2015, **14**, 685–690.

9 J. Wang, J. Liang, Y. Xu, B. Liang, J. Wei, C. Li, X. Mu, K. Ye and Y. Wang, *J. Phys. Chem. Lett.*, 2019, **10**, 5983–5988.

10 D. R. Lee, S. H. Han and J. Y. Lee, *J. Mater. Chem. C*, 2019, **7**, 11500–11506.

11 R. Kabe, N. Notsuka, K. Yoshida and C. Adachi, *Adv. Mater.*, 2016, **28**, 655–660.

12 B. O'Regan and M. Grätzel, *Nature*, 1991, **353**, 737–740.

13 G. Zhou, W.-Y. Wong, S.-Y. Poon, C. Ye and Z. Lin, *Adv. Funct. Mater.*, 2009, **19**, 531–544.

14 J. W. Perry, K. Mansour, S. R. Marder, K. J. Perry, D. Alvarez and I. Choong, *Opt. Lett.*, 1994, **19**, 625–627.

15 S. Baluschev, T. Miteva, V. Yakutkin, G. Nelles, A. Yasuda and G. Wegner, *Phys. Rev. Lett.*, 2006, **97**, 143903.

16 H. Xu, R. Chen, Q. Sun, W. Lai, Q. Su, W. Huang and X. Liu, *Chem. Soc. Rev.*, 2014, **43**, 3259–3302.

17 Z. Xia and A. Meijerink, *Chem. Soc. Rev.*, 2017, **46**, 275–299.

18 S. Tian, H. Ma, X. Wang, A. Lv, H. Shi, Y. Geng, J. Li, F. Liang, Z.-M. Su, Z. An and W. Huang, *Angew. Chem., Int. Ed.*, 2019, **58**, 6645–6649.

19 S. Xu, R. Chen, C. Zheng and W. Huang, *Adv. Mater.*, 2016, **28**, 9920–9940.

20 O. Bolton, K. Lee, H.-J. Kim, K. Y. Lin and J. Kim, *Nat. Chem.*, 2011, **3**, 205–210.

21 W. Zhao, Z. He, J. W. Y. Lam, Q. Peng, H. Ma, Z. Shuai, G. Bai, J. Hao and B. Z. Tang, *Chem*, 2016, **1**, 592–602.

22 L. Huang, B. Chen, X. Zhang, C. O. Trindle, F. Liao, Y. Wang, H. Miao, Y. Luo and G. Zhang, *Angew. Chem., Int. Ed.*, 2018, **57**, 16046–16050.

23 J.-A. Li, J. Zhou, Z. Mao, Z. Xie, Z. Yang, B. Xu, C. Liu, X. Chen, D. Ren, H. Pan, G. Shi, Y. Zhang and Z. Chi, *Angew. Chem., Int. Ed.*, 2018, **57**, 6449–6453.

24 W. Z. Yuan, X. Y. Shen, H. Zhao, J. W. Y. Lam, L. Tang, P. Lu, C. Wang, Y. Liu, Z. Wang, Q. Zheng, J. Z. Sun, Y. Ma and B. Z. Tang, *J. Phys. Chem. C*, 2010, **114**, 6090–6099.

25 M. Fang, J. Yang, X. Xiang, Y. Xie, Y. Dong, Q. Peng, Q. Li and Z. Li, *Mater. Chem. Front.*, 2018, **2**, 2124–2129.

26 G. G. Giachino and D. R. Kearns, *J. Chem. Phys.*, 1970, **52**, 2964–2974.

27 J. Wang, C. Wang, Y. Gong, Q. Liao, M. Han, T. Jiang, Q. Dang, Y. Li, Q. Li and Z. Li, *Angew. Chem., Int. Ed.*, 2018, **57**, 16821–16826.

28 Y. Wen, H. Liu, S. Zhang, Y. Gao, Y. Yan and B. Yang, *J. Mater. Chem. C*, 2019, **7**, 12502–12508.

29 D. R. Kearns and W. A. Case, *J. Am. Chem. Soc.*, 1966, **88**, 5087–5097.

30 T. Itoh, *Chem. Phys. Lett.*, 1988, **151**, 166–168.

31 H. Wang, H. Shi, W. Ye, X. Yao, Q. Wang, C. Dong, W. Jia, H. Ma, S. Cai, K. Huang, L. Fu, Y. Zhang, J. Zhi, L. Gu, Y. Zhao, Z. An and W. Huang, *Angew. Chem., Int. Ed.*, 2019, **58**, 18776–18782.

32 L. Xu, G. Li, T. Xu, W. Zhang, S. Zhang, S. Yin, Z. An and G. He, *Chem. Commun.*, 2018, **54**, 9226–9229.

33 S. Schott, E. R. McNellis, C. B. Nielsen, H. Y. Chen, S. Watanabe, H. Tanaka, I. McCulloch, K. Takimiya, J. Sinova and H. Sirringhaus, *Nat. Commun.*, 2017, **8**, 10.

34 A. Rodriguez-Serrano, V. Rai-Constapel, M. C. Daza, M. Doerr and C. M. Marian, *Phys. Chem. Chem. Phys.*, 2015, **17**, 11350–11358.

35 H. Chen, Y. Deng, X. Zhu, L. Wang, L. Lv, X. Wu, Z. Li, Q. Shi, A. Peng, Q. Peng, Z. Shuai, Z. Zhao, H. Chen and H. Huang, *Chem. Mater.*, 2020, **32**, 4038–4044.

36 D. de Sa Pereira, D. R. Lee, N. A. Kukhta, K. H. Lee, C. L. Kim, A. S. Batsanov, J. Y. Lee and A. P. Monkman, *J. Mater. Chem. C*, 2019, **7**, 10481–10490.

37 D. R. Lee, K. H. Lee, W. Shao, C. L. Kim, J. Kim and J. Y. Lee, *Chem. Mater.*, 2020, **32**, 2583–2592.

38 C. L. Kim, J. Jeong, D. R. Lee, H. J. Jang, S.-T. Kim, M.-H. Baik and J. Y. Lee, *J. Phys. Chem. Lett.*, 2020, **11**, 5591–5600.

39 T. Weng, G. Baryshnikov, C. Deng, X. Li, B. Wu, H. Wu, H. Ågren, Q. Zou, T. Zeng and L. Zhu, *Small*, 2020, **16**, 1906475.

40 A. Mandal, S. Dana, H. Sahoo, G. S. Grandhi and M. Baidya, *Org. Lett.*, 2017, **19**, 2430–2433.

41 L. Xiao, Y. Wu, J. Chen, Z. Yu, Y. Liu, J. Yao and H. Fu, *J. Phys. Chem. A*, 2017, **121**, 8652–8658.

42 Z. Wang, Y. Zhang, C. Wang, X. Zheng, Y. Zheng, L. Gao, C. Yang, Y. Li, L. Qu and Y. Zhao, *Adv. Mater.*, 2020, **32**, 1907355.

43 I. Bhattacharjee and S. Hirata, *Adv. Mater.*, 2020, **32**, 2001348.

44 P. Pander, A. Swist, J. Soloducho and F. B. Dias, *Dyes Pigm.*, 2017, **142**, 315–322.

45 L. Ma, S. Sun, B. Ding, X. Ma and H. Tian, *Adv. Funct. Mater.*, 2021, **31**, 2010659.

46 R. Huang, J. S. Ward, N. A. Kukhta, J. Avó, J. Gibson, T. Penfold, J. C. Lima, A. S. Batsanov, M. N. Berberan-Santos, M. R. Bryce and F. B. Dias, *J. Mater. Chem. C*, 2018, **6**, 9238–9247.

47 Y. Zhou, W. Qin, C. Du, H. Gao, F. Zhu and G. Liang, *Angew. Chem., Int. Ed.*, 2019, **58**, 12102–12106.

48 Y. Wang, B. Li, Y. Liu, L. Zhang, Q. Zuo, L. Shi and Z. Su, *Chem. Commun.*, 2009, 5868–5870.

49 X. Q. Liu, K. Zhang, J. F. Gao, Y. Z. Chen, C. H. Tung and L. Z. Wu, *Angew. Chem., Int. Ed.*, 2020, **59**, 23456–23460.

50 L. Zang and H. Zhao, *RSC Adv.*, 2020, **10**, 32938–32945.

51 Z. Xia, N. Xue, W. Shi and C. Lu, *J. Phys. Chem. C*, 2019, **123**, 30536–30544.

52 R. Keruckiene, D. Volyniuk, K. Leitonas and J. V. Grazulevicius, *Sens. Actuators, B*, 2020, **321**, 128533.